UC San Diego
UC San Diego Electronic Theses and Dissertations

Title
Cloud shadow Speed Sensor (CSS)

Permalink
https://escholarship.org/uc/item/248943hr

Author
Fung, Victor

Publication Date
2014

Peer reviewed|Thesis/dissertation

eScholarship.org Powered by the California Digital Library
University of California

UNIVERSITY OF CALIFORNIA, SAN DIEGO

Cloud shadow Speed Sensor (CSS)

A thesis submitted in partial satisfaction of the requirements
for the degree Master of Science

in

Engineering Sciences (Mechanical Engineering)

by

Victor Fung

Committee in Charge:

Professor Jan Kleissl, Chair
Professor David Benson
Professor Carlos F.M. Coimbra

2014

The thesis of Victor Fung is approved and acceptable in quality and form for publication on microfilm and electronically:

Chair

University of California, San Diego

2014

TABLE OF CONTENTS

Signature Page iii
Table of Contents iv
List of Figures v
List of Tables vi
Acknowledgements vii
Abstract of the Thesis ix
1 Introduction 1
2 Theory: Most Correlated Pair Method (MCP) 4
3 Cloud Shadow Speed Sensor (CSS) 6
3.1 Luminance Sensors 6
3.2 Luminance Sensor Array 7
3.3 Data Acquisition and Post-Processing 9
3.4 Performance Parameters and Limitations 11
3.5 Validation using Artifical Shadows 12
3.6 Deployment and Validation Against Two Cloud Motion Sensors 14
4 Results and Discussion 15
5 Conclusions 21
References 22

LIST OF FIGURES

Figure 1: Idealized sketch showing the most correlated pair of signals shifted by t_{ab} (adapted from Bosch et al., 2013). 4

Figure 2: Cloud shadow Speed Sensor (CSS). The entire system is contained inside a weather proof enclosure. On the top of the enclosure is an array of nine phototransistors used to measure the variation in solar radiation as clouds passed overhead. 6

Figure 3: Simplified schematic showing excitation voltage applied to the phototransistor collector, the 2 *k*Ω load resistor, and the sensor output as applied to an analog input channel on the microcontroller. 7

Figure 4: Luminance sensor arrangement. Each circle represents a sensor arranged in a circular pattern with 15° radial spacing about the central sensor. Additional angles from 120° to 165° are obtained through equilateral triangles constructed from existing sensor positions. For example, for triangle *abc* the line from *b* to *c* results in an angle of 120°. 8

Figure 5: Cross-sectional view of luminance sensor optical assembly (TEPT4400, opaque tube, and light collector/diffuser) for a vertical spacing *h* that matches the TEPT4400 field of view (FOV) to the diffuser diameter. To reduce the effect of TEPT4400 sensor tilt errors, *h* = 2.98 mm was chosen instead. 9

Figure 6: Solar irradiance and CMVs from CSS, USI, and LCE for 23 July. Luminance measurements of the central TEPT4400 sensor were calibrated against a co-located pyranometer to obtain W m^{-2} of solar irradiance. 17

Figure 7: Sky images on 23 July 2013: (a) 1300 PST, (b) 1400 PST. Overcast observed after 1400 PST persisted for the remainder of the day. 18

Figure 8: Solar irradiance and CMVs detected during the CSS deployment on 8 August 2013 ... 19

LIST OF TABLES

Table 1: CSS performance for the artificial cloud shadow experiment. 13

Table 2: Deployment dates and average direction and speed for each cloud motion sensor. USI CMVs are unavailable for 14 March and 10 May due to incorrect cloud heights. LCE results are removed on 23 April due to an insufficient amount of results that passed QC..... 15

Table 3: RMSD and MB of CSS results compared to LCE and USI. Due to incorrect cloud height observed, no cloud motion results were detected from USI on 14 March and 10 May. LCE results are excluded for 23 April due to a deficient amount of results passing QC. 16

ACKNOWLEDGEMENTS

I would like to acknowledge Professor Jan Kleissl and PostDoc Juan L. Bosch for their guidance, advice, and insight that led to the breakthrough of many hardware and software issues throughout the development of the cloud shadow speed sensor. I am thankful for the time Prof. Kleissl spent on correcting my reports, paper, and thesis, which had indirectly taught me how to write more effectively, format plots and figures properly, and much more. Prof. Kleissl had provided tremendous support in data interpretation and linkage to atmospheric science as well. In addition, I am grateful to mentor Juan L. Bosch for his support in data analysis, MatLAB and C++ programming help, and other software related issues. Juan helped to find ways on improving the system in robustness, efficiency, performance, quality, and etc.

Additionally, I would like to acknowledge another mentor, Steve Roberts, for his guidance on electronics and experimental procedure. Steve prepared the setup of multiple experiments and provided electrical components and tools to assist with testing and development. Alongside Steve, I must also thank Nick Busan, Mike Watson, Tom Chalfant, Isaiah Freerksen, and Chris Cassidy (generally the MAE staff core) for providing access to equipment, experimental facility, machine tools, time, effort, knowledge, and much more.

Lastly, this project is grateful to (i) Tyler L. Capps, Andy Chen, Jeff Head for assisting with initial hardware prototype and software developemnt, (ii) Ben Kurtz, Andu Nguyen, Bryan Urquhart, Elliot Dahlin, Mohamed Ghonima, Chi Wai Chow, Handa Yang, and Felipe Mejia for constructing and operating the UCSD sky imager, (iii)

Dominic Fong, Edward Matios, E. Lauren Cwiklo, Nancy Ronquillo, and Atalie Dajani for carrying out test procedures and analysis to characterize cloud speed sensor components.

Without those mentioned above, the cloud speed sensor would not have developed, matured, and accomplished as much as it has today.

Chapter 1, in part, has been submitted for publication of the material as it may appear in Atmospheric Measurement Techniques (AMT), 2014, Fung, Victor; Bosch, Juan L.; Roberts, Stephen W.; Kleissl, Jan, Copernicus Publications, 2014. The thesis author was the primary investigator and author of this paper.

Chapter 2-5, in full, has been submitted for publication of the material as it may appear in Atmospheric Measurement Techniques (AMT), 2014, Fung, Victor; Bosch, Juan L.; Roberts, Stephen W.; Kleissl, Jan, Copernicus Publications, 2014. The thesis author was the primary investigator and author of this paper.

ABSTRACT OF THE THESIS

Cloud shadow Speed Sensor (CSS)

by

Victor Fung

Master of Science in Engineering Sciences (Mechanical Engineering)

University of California, San Diego, 2014

Professor Jan Kleissl, Chair

Changing cloud cover is a major source of solar radiation variability and poses challenges for the integration of solar energy. A compact and economical system that measures cloud shadow motion vectors to estimate power plant ramp rates and provide short-term forecasting is presented. The Cloud shadow Speed Sensor (CSS) is constructed using an array of luminance sensors and a high-speed data acquisition system to resolve the progression of cloud passages across the sensor footprint. An embedded microcontroller acquires the sensor data and uses a cross-correlation algorithm to determine cloud shadow motion vectors. The CSS was validated against an artifical

shading test apparatus, an alternative method of cloud motion detection from ground-measured irradiance (linear cloud edge, LCE), and a UC San Diego sky imager (USI). The CSS detected artifical shadow directions and speeds to within 15° and 6 % accuracy, respectively. The CSS detected (real) cloud shadow directions and speeds with average weighted root-mean-square difference of 22° and 1.9 m s^{-1} when compared to USI and 33° and 1.5 m s^{-1} when compared to LCE results.

1 INTRODUCTION

Increasing global energy consumption and greenhouse gas emissions are major concerns on world energy outlook and climate. Fossil fuels make up for approximately 87 % of global energy production while contributing about 36 billion tons (and increasing) of additional carbon dioxide to the atmosphere. In order to reduce global dependency on fossil fuels, there has been an increased investment and implementation of zero-carbon renewable energy sources, such as solar and wind power.

Solar resource is most abundant and is orders of magnitude greater than all other renewable sources combined. On average, the sun emits 174 petaWatts or approximately 8000 times more energy than total global energy consumption; making solar power a strong candidate for supplying future world energy needs with minimal greenhouse gas emissions. In fact, harvesting solar energy at 100% absorption for approximately 1.5 hrs will provide enough energy to meet global demand for an entire year. However, difficulties in integrating variable generators into the electric grid have impacted the rate of large-scale adoption of solar power. The variability of the solar resource could be better accomodated by grid operators if fluctuations in irradiance caused by cloud cover could be predicted.

Understanding cloud motion is critical for ramp rate estimation and short-term forecasting (Arias-Castro et al., 2013; Coimbra et al., 2013; Lave et al., 2012, 2013), since moving clouds attenuate solar radiation at the Earth's surface and causes spatiotemporal solar power variability at ground level. As a result, varying cloud cover can cause sudden deficiency or oversupply in solar power that can compromise grid stability and must be compensated with an opposing ramp of energy storage or

conventional generation. Previous studies have used satellite imagery for estimating cloud motion (Leese et al., 1971; Hammer et al., 1999; Lorenz et al., 2004; Perez et al. 2010), but due to satellite navigation, resolution, and parallax uncertainties, such cloud motion estimates are of limited use in short-term, intra-hour forecasting.

Other methods determine cloud *shadow* speed using ground-based solar radiation measurements. Cloud shadow motion vectors are typically equivalent to cloud motion vectors as measured from satellites or simulated through numerical weather prediction (since Sun—Earth distance >> cloud—Earth distance), but large solar zenith angles or large cloud vertical development relative to horizontal translation can introduce differences. While cloud shadow speed may not be as useful as horizontal cloud speed for meteorological models, cloud shadow motion vectors are more relevant for ground-based solar forecasting applications. For the remainder of the paper, ‘cloud speed’ or ‘cloud motion vector’ measurements will be used for conciseness, although strictly cloud shadow motion vectors are measured. Examples of cloud speed detection from ground sensors are given in Hinkelman et al. (2011), who determined cloud speeds by analyzing the time lag in maximum cross-correlation between two sensors aligned with the cloud direction, but the method cannot be automated since cloud direction has to be known a priori. Weigl et al. (2012) also derived velocity vectors from spatial irradiation data by considering rectangular clouds and tracking the movement of irradiation minima across the sensor array. Recently, two different approaches to determine cloud motion vectors were developed and validated by Bosch et al. (2013) using ground-based solar radiation measurements. The first approach (further developed in Bosch and Kleissl, 2013) considers the kinematic equations of a linear cloud edge (LCE) passing through a sensor

triplet and will be used in this paper for validation. The second method is based on the most correlated pair (MCP) of sensors arranged in 12 m diameter semi-circular array and lays the foundation of the Cloud shadow Speed Sensor (CSS) described here. However, the limited sampling frequency requires sensor spacings of tens of meters and does not permit detecting cloud speeds with enough resolution to cover the full range of naturally occurring cloud speeds. Also, the system is not self-contained and cannot perform on-board post-processing. A semicircle system that is smaller, self-contained, and sampling at high frequency is more appropriate for commercial use and is described in this paper.

Section 2 introduces the theoretical concept of the cloud motion vector (CMV) measurement. Sections 3.1 and 3.2 describes the phototransistor characteristics, optical assembly, and layout. In Sect. 3.3 the data acquisition and post-processing system is presented and quality control is discussed. Performance parameters and limitations of the CSS are explained in Sect. 3.4. Validation procedures for the algorithm and cloud motion results against artificial shadows and (real) clouds are discussed in Sects. 3.5 and 3.6. Results of the validation are presented in Section 4.

2 THEORY: MOST CORRELATED PAIR METHOD (MCP)

Variability of solar irradiance on the Earth's surface is mainly due to cloud shadows with varying light intensity. A system to obtain CMVs using an array of ground-based luminance sensors to measure the spatiotemporal variation of solar irradiance over the extent of the sensor array is presented. Using the MCP method described in Bosch et al. (2013), the largest similarity in a pair of signal indicates alignment with the cloud motion direction and is determined by the cross-correlation coefficient $R_{ab}(\Delta t)$:

$$R_{ab}(\Delta t) = \frac{1}{n-1}\sum_{m=1}^{n}\left(\frac{L_{a,t}(m)-\bar{L}_{a,t}}{\hat{L}_{a,t}}\right)\left(\frac{L_{b,t+\Delta t}(m)-\bar{L}_{b,t+\Delta t}}{\hat{L}_{b,t+\Delta t}}\right) \quad (1)$$

where a and b are sensor indices, n is the number of sample points, t and $t + \Delta t$ are the time and lagged time, L_a and L_b are solar irradiance time series, overbars indicate averages and hats represent standard deviations.

Assuming sensors S_a and S_b are the pair with largest R_{ab}, the solar irradiance time series will be most similar, but will be delayed by a time lag, $\Delta t = t_{ab}$, as seen in Fig. 1.

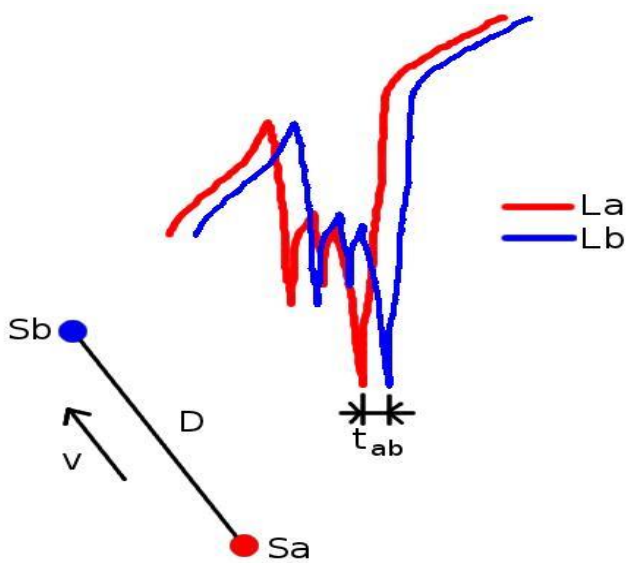

Figure 1. Idealized sketch showing the most correlated pair of signals shifted by t_{ab} (adapted from Bosch et al., 2013).

Determining the time lag via cross correlation, the cloud speed can be found by

$$V_{cloud} = \frac{D}{t_{ab}} \tag{2}$$

where D is the distance separating the sensors.

3 CLOUD SHADOW SPEED SENSOR (CSS)

The CSS (Fig. 2) design objectives are compactness, fast data acquisition rates, robustness, and on-board processing. The implementation includes a high-performance microcontroller platform with built-in data acquisition and storage capability, and an array of phototransistors. The following subsections describe the system in more detail.

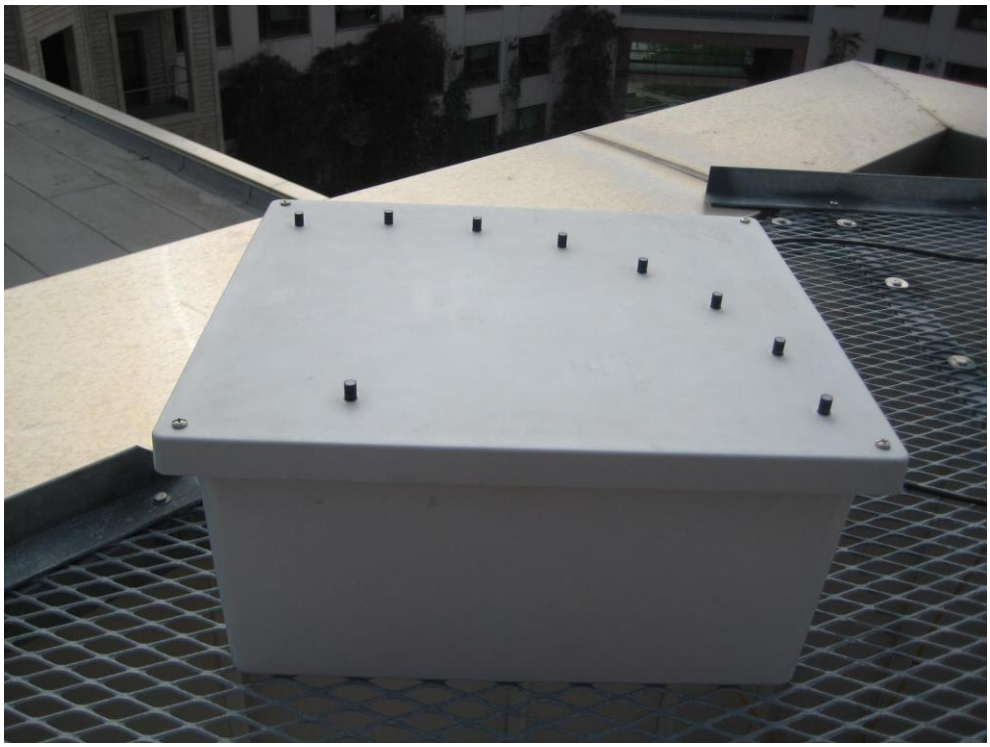

Figure 2. Cloud shadow Speed Sensor (CSS). The entire system is contained inside a weather proof enclosure. On the top of the enclosure is an array of nine phototransistors used to measure the variation in solar radiation as clouds passed overhead.

3.1 LUMINANCE SENSORS

Solar radiation sensors consist of an array of nine phototransistors (TEPT4400, Vishay Intertechnology, Inc., USA). The sensors have a spectral response ranging from approximately 350 to 1000 nm with peak sensitivity at 570 nm. The manufacturer has characterized the sensors over an operating temperature range of –40 to +85°C. Sensor

response time was determined experimentally in a laboratory controlled environment and was found to be 21 μs rise time (10-90% response). Excitation voltage for the sensors was 3.3 VDC supplied from a linear voltage regulator (LM2937-3.3, Texas Instruments, Inc., USA) and applied to the phototransistor collector (Fig. 3). A 2 *kΩ* load resistor was connected from the sensor emitter to system ground. The sensors output were taken at the emitter—load-resistor junction and fed to the analog input channels on the microcontroller.

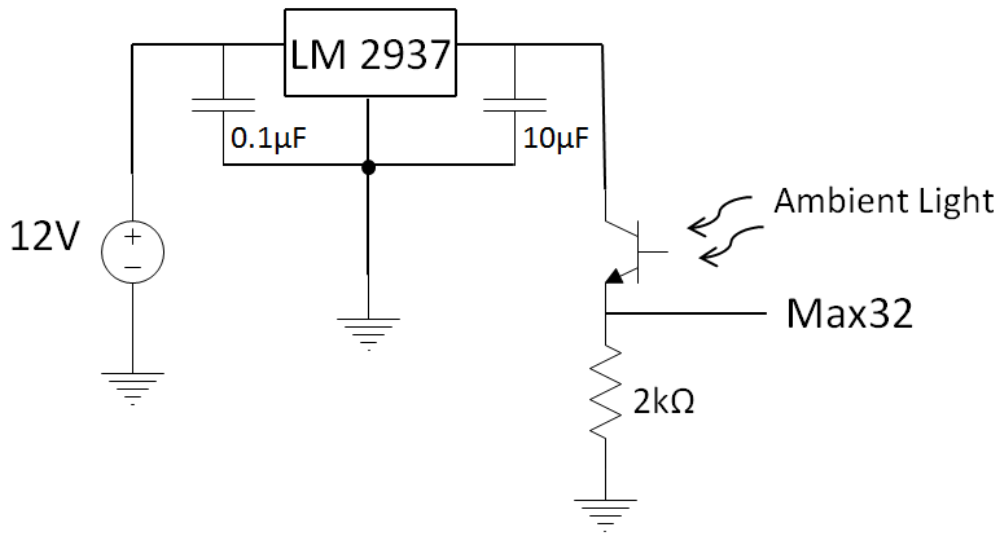

Figure 3. Simplified schematic showing excitation voltage applied to the phototransistor collector, the 2 *k*Ω load resistor, and the sensor output as applied to an analog input channel on the microcontroller.

3.2 LUMINANCE SENSOR ARRAY

CMVs were determined with phototransistors configured as an array of eight sensors positioned around a central sensor on a circle of radius 0.297 m, covering 0-105° in 15° increments (Figs. 2 and 4). Cross-correlation coefficients were computed for each

pair of sensors (central sensor and a sensor on the circle) to determine cloud speed and direction based on Eqs. (1) – (2).

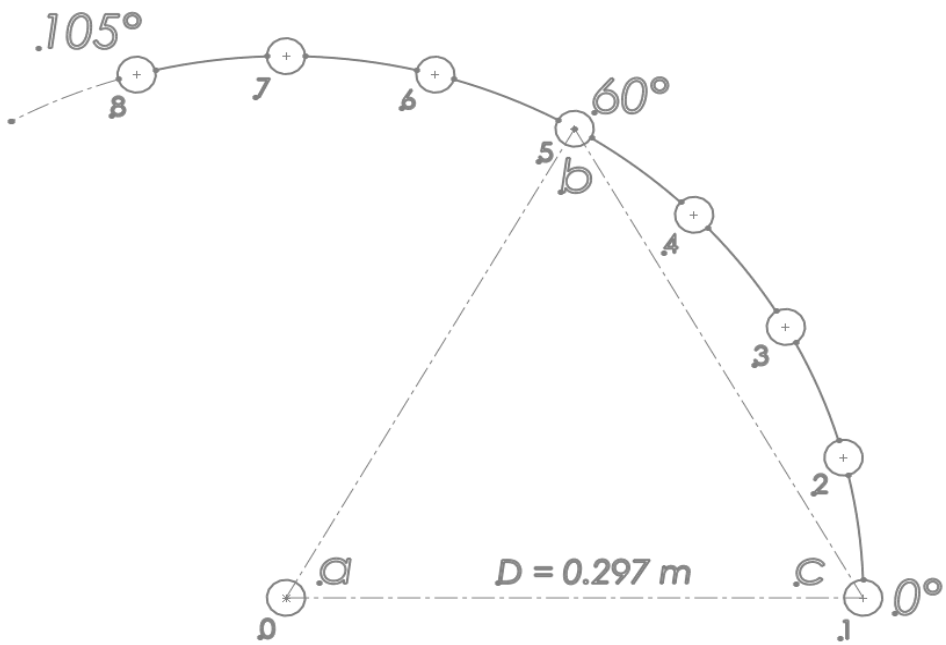

Figure 4. Luminance sensor arrangement. Each circle represents a sensor arranged in a circular pattern with 15° radial spacing about the central sensor. Additional angles from 120° to 165° are obtained through equilateral triangles constructed from existing sensor positions. For example, for triangle *abc* the line from *b* to *c* results in an angle of 120°.

Each sensor was placed at the base of and inside a black opaque tube with a diameter of 6.35 mm and height of 14.3 mm with a translucent acrylic light diffuser/collector at the top. The tube height was chosen such that the diffuser positioned above the sensor fully occupies the TEPT4400 field of view (FOV) as shown in Fig. 5. Full exposure of the TEPT4400 FOV to the overhead light field dictates a vertical separation of $h < 5.51$ mm, but $h = 2.78$ mm was chosen in the design such that a tilt error of up to 18.8° would still allow the TEPT4400 FOV to remain within the diffuser area. This sensor optical assembly (TEPT4400, tube, diffuser) ensures that the CSS has a near-cosine response over the full –90 to 90° exposure to radiation from the full-sky

hemisphere. When tested under halogen lights the diffuser was determined to have no effect on the incident light spectrum within the spectral response range of the sensor.

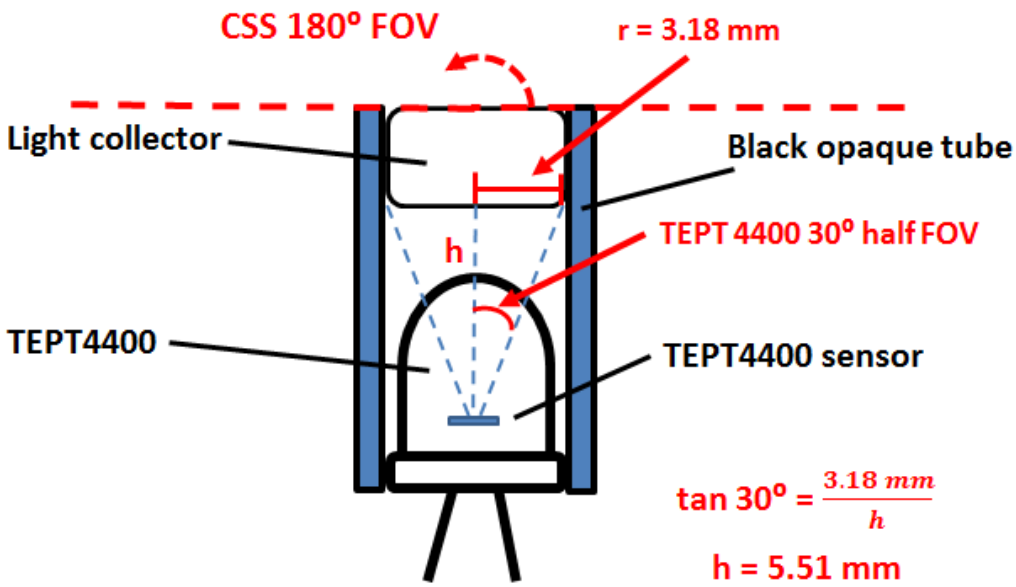

Figure 5. Cross-sectional view of luminance sensor optical assembly (TEPT4400, opaque tube, and light collector/diffuser) for a vertical spacing *h* that matches the TEPT4400 field of view (FOV) to the diffuser diameter. To reduce the effect of TEPT4400 sensor tilt errors, *h* = 2.98 mm was chosen instead.

3.3 DATA ACQUISITION AND POST-PROCESSING

A compromise had to be made between measurement precision and detectable irradiance range due to the limited 10 bit analog-to-digital converter of the microcontroller. Hence, the TEPT4400 circuit was deliberately designed to report voltages that exceed the measurement range of the microcontroller near solar noon on clear days. In particular, the detected solar irradiance saturates at 880 W m^{-2} but higher irradiance can be neglected since near clear-sky periods are rejected for post-processing due to small variance. Irradiance measurements under 880 W m^{-2} representing cloudy conditions are therefore better resolved and more appropriate for CSS application.

The microcontroller-based data acquisition system and luminance sensors are powered by a small rechargable 12 VDC sealed lead—acid battery. Regulated voltages (5 VDC for the microcontoller, 3.3 VDC for the sensors) are derived from the battery using integrated circuit linear voltage regulators (Fig. 3). The data acquisition system was configured using a high-performance 32 MIPS, 32 bit microcontroller platform (chipKIT Max32, Digilent Inc., USA) clocking at 80 MHz. The on-board static memory allows fast storage of up to 6000 10 bit data points per sensor. With a sampling rate of 667 samples s^{-1}, 6000 data points can be acquired and stored in approximately 9 s. The 6000 x 9 data matrix can be transferred to an off-board microSD card in 1 s, for archiving and further analysis.

Alternatively, on-board post-processing is available and the results can be relayed to a central computer via Ethernet or wireless communication. The cloud speed and direction are determined using an algorithm based on Eqs. (1) – (2). Computing the cross-correlation for every time step (i.e. m = 1 to 5600 in 400 steps) would require 18 min. Optimization reduced the processing duration to approximately 23 s. First, assuming a monotonous "smooth" signal, the cross-correlation time shift is performed in increments of 40 time steps instead of the standard 1 time step. Then, the local maximum R_{ab} is located and the surrounding 80 R_{ab} are subsampled in time steps of 10. This procedure is repeated with subsampling local R_{ab} in 4 time steps and then 1 time step to determine the exact t_{ab} corresponding to the global maximum R_{ab}. Second, $\bar{L}_b$ and $\hat{L}_b$ of each R_{ab} are updated based on the previous $\bar{L}_b$ and $\hat{L}_b$. Third, only 5 sensor pairs with largest local maximum R_{ab} after subsampling in 40 time steps will be selected for additional

subsampling produces. Through extensive post-processing analysis this algorithm has proven to be robust in finding t_{ab}.

Quality control (QC) during post-analysis is required to increase the robustness of the algorithm (Bosch et al., 2013). Most importantly, periods of small variability in the signal (for example during near clear-sky conditions) or small correlation coefficients are excluded. In specific, the range in a set of measurements must exceed 7% of the full-scale 10 bit reading and the largest R_{ab} computed must exceed 0.95. Both threshold values were determined empirically, and they ensure the measurement time series captured a cloud passage period which results in large signal-to-noise ratio and is more likely to produce correct CMVs. Measurements with several identical maximum R_{ab} across different sensor pairs or unphysical cloud speeds (greater than 50 m s^{-1} is very unlikely) are also discarded. Lastly, a moving median filter is computed at every CMV timestamp to determine the central tendency of QC results within the past 30 min. While there is a potential to delay the detection of a change in cloud motion, CMVs generally change over longer time scales.

In addition to CMV detection, variability in solar irradiance can be measured by the CSS and could be used by grid operators to inform control schemes for energy storage or rampable generation throughout the day.

3.4 PERFORMANCE PARAMETERS AND LIMITATIONS

Based on typical cloud speeds obtained over the US (Bosch and Kleissl, 2013; Lave et al., 2013a), the CSS was designed to detect cloud speeds of up to 15 m s^{-1} with at least 1 m s^{-1} resolution. The resolution of detectable cloud speeds is determined by the

radius of the semicircle (D = 0.297 m, Eq. 2) and the sampling time step (Δt = 0.0015 s). For the CSS design, the resolvable cloud speeds are given by $\frac{D}{N\Delta t}$, where N = 1, …, k and k defines the maximum number of time shifts used in the cross-correlation computations. In this case we select the minimum cloud speed as 1 m s^{-1}, which yields k = 200. Cloud speeds of less than 1 m s^{-1} are unusual and have little relevance to solar power as the resulting ramp rates would be slow and approach the cloud lifetime (Jiang et al., 2006). With 6000 samples from each sensor, the central 5600 data points are shifted in the cross correlation procedure, leaving 200 bidirectional time shifts to determine t_{ab}. The direction of the shift that produces the global maximum R_{ab} indicates whether the clouds are moving in one direction or the opposite. The largest and smallest resolvable cloud speeds are therefore $\frac{D}{\Delta t} = \frac{0.297\text{m}}{0.0015s} = 198.1$ m s^{-1} and $\frac{D}{k\Delta t} = \frac{0.297\text{m}}{200 \cdot 0.0015s} = 0.99$ m s^{-1}, respectively. The cloud speed resolution scales with $\frac{1}{N}$ such that very large cloud speeds are obtained at poor resolution (for example the second largest speed is $\frac{0.297\text{m}}{2 \cdot 0.0005s} = 99.1$ m s^{-1}) while smaller cloud speeds can be detected at higher resolution.

3.5 VALIDATION USING ARTIFICAL SHADOWS

Prior to measuring complex ground radiation patterns caused by clouds, a preliminary performance test with a simple shadow of known relative velocity was tested on the CSS. Under clear conditions at solar noon, an irregular stationary shadow was created from a suspended object. The CSS was mounted on a mobile platform that was pulled at a constant speed by a torque motor. Relative velocity vectors between the shadow and sensor can be determined by the motor rotational speed and orientation of the

sensor. The magnitude of the irradiance reduction (i.e. the signal for Eq. 1) in the shadow decreases with increasing height of the object due to increased diffuse irradiance. Consequently, the CSS was first tested with a dark shadow from an object positioned 0.23 m above the CSS. The CSS was moved at a known CSS speed of 0.51 m s^{-1} with different directions (60 and 90°). Since the known CSS speed did not fall within the range of detectable cloud speeds (see Sect. 3.4), k = 600 was used to reduce the smallest resolvable cloud speed to 0.33 m s^{-1} for this experiment. The procedure was repeated with the object raised to 1.35 m above the CSS to observe how the influence of increased diffuse irradiance affects the measurements, post-processing, and CMVs.

Table 1. CSS performance for the artificial cloud shadow experiment.

Height of Object above CSS	**True direction [°]**	**CSS direction [°]**	**True speed [m s^{-1}]**	**CSS speed [m s^{-1}]**
0.23 m	60	60	0.51	0.48
0.23 m	90	105	0.51	0.48
1.35 m	60	60	0.51	0.48
1.35 m	270	270	0.51	0.48

For all conditions, the detected directions were correctly identified and the detected shadow speed fell within 6% of the true speed (Table 1), which is acceptable for CSS application. The only direction error occurred in experiment 2, but the maximum R_{ab} values for the 90 and 105° directions were essentially indistinguishable with a difference of 0.0006. These results validate the basic concept, realization, and algorithm of the CSS to measure (real) cloud speed and direction.

3.6 DEPLOYMENT AND VALIDATION AGAINST TWO CLOUD MOTION SENSORS

The CSS was deployed on nine days over a period of six months from March to August 2013 at the UC San Diego Solar Energy test bed in La Jolla, CA (Table 2). For validation, a sky imager was deployed adjacent to the CSS and a consistent coordinate system was established. The UCSD Sky Imager (USI, Chow et al., 2011; Urquhart et al., 2013; Yang et al., 2013), captures images using an upward-facing charge-coupled device (CCD) image sensor sensing RGB channels at 12 bit precision and 1748 x 1748 pixel resolution. A 4.5 mm circular fisheye lens allows imaging the entire sky hemisphere. Utilizing composite high dynamic range (HDR) imaging, the USI outputs images at 16 bit with a dynamic range of 84 dB. The images used in this analysis were taken by a rooftop-mounted USI located at 32.8722°N, 117.2410°W, and 129 m m.s.l. capturing images every 30 s. A cross-correlation method is applied to derive a representative cloud vector for the image (Yang et al., 2013).

USI cloud directions are expected to be accurate, but cloud speeds scale linearly with cloud height which is difficult to determine. Therefore the LCE approach (see introduction and Bosch et al., 2013; Bosch and Kleissl, 2013) was applied to three photodiode pyranometers (Li-200SZ, Licor, Inc.). The pyranometers were co-located on the USI rooftop and setup in an orthogonal coordinate system with average separation of 7 m and logged to a single CR1000 (Campbell Scientific Inc.) datalogger with an acquisition frequency of 20 Hz.

4 RESULTS AND DISCUSSION

The predominant cloud conditions in coastal southern California are overcast stratocumulus and few to scattered cumulus clouds. Table 2 shows the average cloud directions and speeds on the nine deployment days. Table 3 presents the corresponding root-mean-square difference (RMSD) and mean bias (MB).

Table 2. Deployment dates and average direction and speed for each cloud motion sensor. USI CMVs are unavailable for 14 March and 10 May due to incorrect cloud heights. LCE results are removed on 23 April due to an insufficient amount of results that passed QC.

	Deployment [PST]	**Average Direction [°]**			**Average Speed [m s^{-1}]**		
Date in 2013	*All Methods*	*CSS*	*LCE*	*USI*	*CSS*	*LCE*	*USI*
14 Mar	1030 - 1615	310	300	--	4.9	5.8	--
16 Mar	1415 - 1800	243	230	252	4.4	3.6	5.3
23 Apr	1000 - 1700	136	--	149	3.3	--	3.2
10 May	1345 - 1745	294	265	--	4.4	4.7	--
14 May	1010 - 1810	281	264	279	5.2	4.7	5.1
3 Jun	1250 - 1850	160	175	182	5.7	5.8	3.4
23 Jul	1200 - 1800	300	275	286	4.8	5.3	3.9
7 Aug	1135 - 1735	301	319	299	4.5	5.5	4.6
8 Aug	1030 - 1730	299	283	286	5.2	4.7	4.3

Table 3. RMSD and MB of CSS results compared to LCE and USI. Due to incorrect cloud height observed, no cloud motion results were detected from USI on 14 March and 10 May. LCE results are excluded for 23 April due to a deficient amount of results passing QC.

	RMSD				**MB**			
	Direction [°]		Speed [m s^{-1}]		Direction [°]		Speed [m s^{-1}]	
Date in 2013	*LCE*	*USI*	*LCE*	*USI*	*LCE*	*USI*	*LCE*	*USI*
14 Mar	41	--	3.0	--	8	--	-0.7	--
16 Mar	25	24	0.9	1.3	-8	-8	0.9	-0.9
23 Apr	--	20	--	0.6	--	-13	--	0.1
10 May	38	--	1.5	--	31	--	-0.6	--
14 May	24	20	0.9	2.5	13	1	0.4	-0.4
3 Jun	20	26	0.6	2.4	-15	-22	-0.2	2.2
23 Jul	35	14	1.2	1.2	25	14	-0.4	0.9
7 Aug	41	7	1.4	2.1	-18	2	-1.0	-0.2
8 Aug	37	26	1.3	0.9	13	13	0.4	-0.2
All	33	22	1.5	1.9	9	-0.7	-0.1	0.2

The 23 July and 8 August deployments are selected for discussion in greater detail. The KNKX METAR station 9 km to the east of UC San Diego reported the following conditions: the air temperature during the 23 July and 8 August deployments was 22–26°C and 24–25°C, respectively. Surface winds were 260 to 310° at 4.1 to 5.7 m s^{-1} on 23 July and 250 to 280° at 3.6 to 4.6 m s^{-1} on 8 August. There were few clouds at 400 m below scattered clouds at 900 to 1200 m a.g.l. on 23 July and few clouds at 460 m a.g.l. on 8 August.

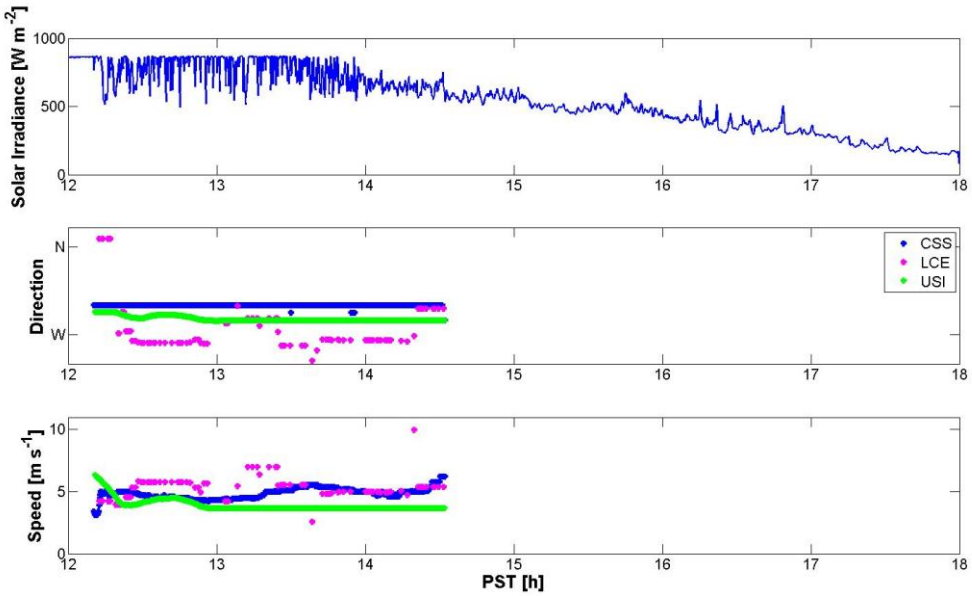

Figure 6. Solar irradiance and CMVs from CSS, USI, and LCE for 23 July. Luminance measurements of the central TEPT4400 sensor were calibrated against a co-located pyranometer to obtain W m^{-2} of solar irradiance.

The solar irradiance and resultant CMVs for 23 July and 8 August are shown in Figs. 6 and 8. For 23 July, 20 % of the 1611 raw results satisfy the QC criteria described in Sect. 3.3; most results are excluded since the variability did not exceed 7 % of 10 bit full-scale reading, as observed after 14:00 PST. Sky imagery reveals that CMV results occurred in scattered stratocumulus cloud cover during 12:00–14:00 PST that became overcast after 14:00 PST (differences to the METAR cloud observations can be explained by large spatial heterogeneity of cloud cover in this coastal area) as seen in Fig. 7. Despite the overcast conditions, the visibility of the solar corona behind the clouds indicates that the observed clouds were thin and transmitted higher solar irradiances than one would typically expect under low overcast skies. Overcast conditions cause insufficient solar variability to pass the QC criteria, but the 30 min median filter causes CMV to persist into the overcast period, like during 14:00–14:30 PST. The CSS QC

directions indicate cloud movement from the west-northwest (WNW, 300°) direction, consistent with surface winds and visual inspection of sky imagery. USI and LCE results show an average cloud motion direction of 286 and 275° with RMSDs of 14 and 35°, respectively. The CSS cloud speed ranges from 3.0 to 6.0 m s^{-1}. USI and LCE yield an average cloud speed of 3.9 and 5.3 m s^{-1}, with RMSD of 1.2 and 1.2 m s^{-1} compared to CSS results, respectively.

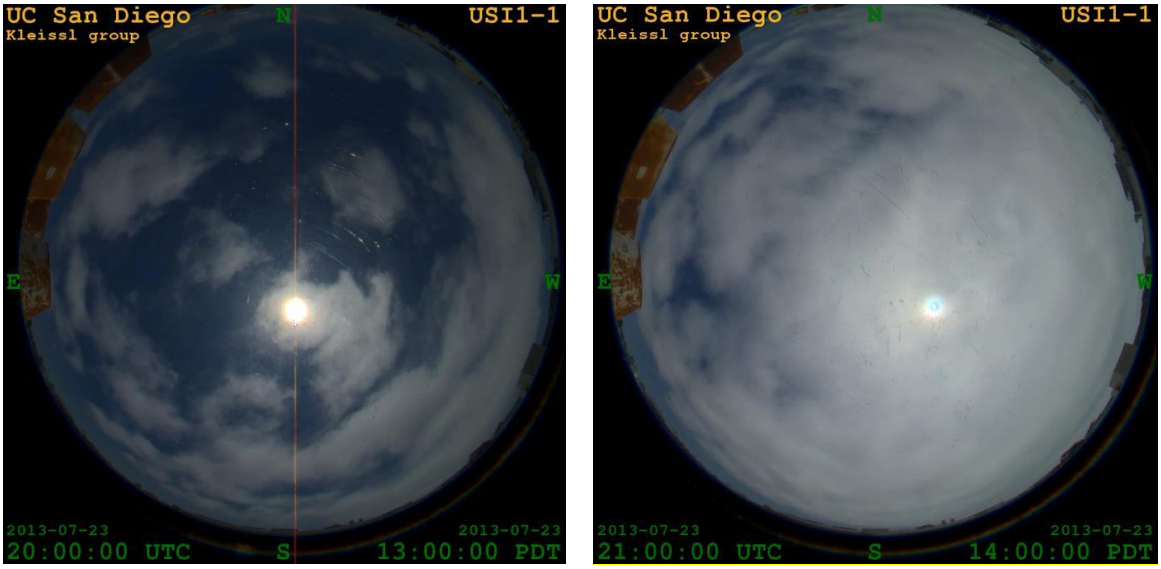

(a) **(b)**

Figure 7. Sky images on 23 July 2013: (a) 1300 PST, (b) 1400 PST. Overcast observed after 1400 PST persisted for the remainder of the day.

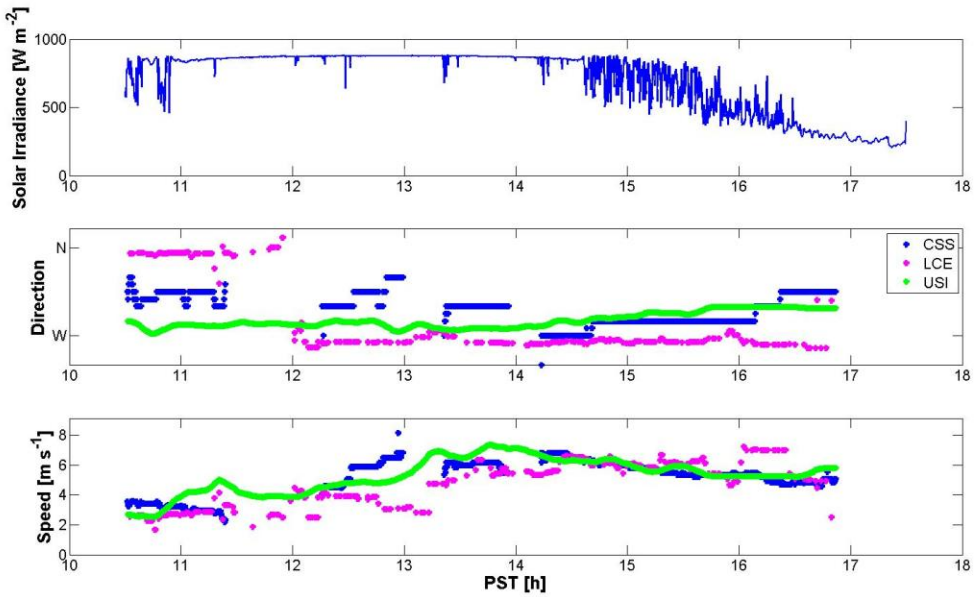

Figure 8. Solar irradiance and CMVs detected during the CSS deployment on 8 August 2013.

On 8 August, visual inspection from sky imagery shows thin, scattered stratocumulus clouds during 10:30–14:45 PST from WNW that became more widespread during 14:45–16:30 PST. Overcast conditions occurred after 16:30 PST, which causes low solar irradiance variability and again produces no CMV results. The CSS detects average cloud movement from the WNW (299°) direction, while USI and LCE detect average cloud directions of 286 and 283°, respectively. RMSD values for comparing CSS to USI and LCE direction results are 26 and 33°, respectively. The CSS cloud speed increases from 2.0 to 6.8 m s^{-1} throughout the deployment and is consistent with the range and trends observed by USI and LCE with RMSD of 0.9 and 1.3 m s^{-1}, respectively. It is worth noting that all speed results are similar during periods of high solar variability (14:45–16:00 PST), which indicates more robustness during favorable cloud conditions. Although the three methods slightly differ in both detected direction

and speed, the results are within acceptable CSS, USI, and LCE method uncertainty. True cloud speeds are not available and it is therefore unclear which sensor is more accurate.

The post-analysis conducted on days presented in Tables 2 and 3 assumes a single layer of cloud movement. In the presence of multilayer clouds, several regions with high density of CMVs can be found at different cloud velocities. By using a histogram peak-finding technique on QC CMV results, the CSS can determine multilayer cloud movement. This method was based on prior research on CMV determination from ground irradiance data and requires further analysis, but should be feasible to implement in the CSS algorithm for identifying multilayer CMVs. Cloud motion experiencing wind shear can have a vertical speed component that is undetectable by the CSS. However, the CSS will detect 2-D cloud shadow motion (x–y plane) in scenarios with 3-D cloud movement. While this measurement may not be as useful for meteorological models, the cloud shadow speed is more relevant to provide for solar variability and forecasting applications. The analysis presented in Tables 2 and 3 also shows comparable results between CSS, USI, and LCE results for a wide range of cloud directions (southeasterly to northwesterly). The range of cloud speeds is more limited due to the low cloud heights and benign weather conditions in coastal southern California, but results are again consistent with the other methods. Overall speed and direction biases are essentially zero and typical RMSDs are 2 m s^{-1} and 30°.

5 CONCLUSIONS

Nine phototransistors arranged in a semicircular formation were used to obtain cloud shadow motion vectors by finding the maximum signal cross correlation between the different pairs of sensors. Fast sampling rates by the microprocessor allowed the system to be compact yet able to detect typical cloud speeds from 1 to 15 m s^{-1} (with 1 m s^{-1} precision) and up to 24 m s^{-1} with 2 m s^{-1} precision. The CSS was validated using an artificial shading test apparatus and was found to detect cloud directions and speeds to within 15° and 6% accuracy, respectively. Nine deployments on partly cloudy days resulted in cloud directions and speed consistent with those observed from a sky imager and computed from the LCE method. Unlike the prior proof of feasibility in Bosch et al. (2013), the present CSS system is self-contained and more economical while still producing accurate cloud motion vectors. With the present QC criteria, the CSS does not provide CMV results under near uniform overcast conditions, but the small solar irradiance variability in overcast conditions does not present a major issue for solar power integration. Further optimization of the algorithm will refine QC procedures to retain as many CMVs as possible while ensuring robustness of the results.

REFERENCES

Arias-Castro, E., Kleissl, J., Lave, M., Schweinsberg, J., and Williams, R.: A Poisson model for anisotropic solar ramp rate correlations, Solar Energy, 101:192-202, 2014.

Bosch, J. L. and Kleissl, J.: Cloud motion vectors from a network of ground sensors in a solar power plant, Sol. Energy, 95, 13–20, 2013.

Bosch, J. L., Zheng, Y., and Kleissl, J.: Cloud velocity estimation from an array of solar radiation measurements, Solar Energy, 87, 196–203, doi:10.1016/j.solener.2012.10.020, 2013.

Chow, C. W., Urquhart, B., Kleissl, J., Lave, M., Dominguez, A., Shields, J., and Washom, B.: Intra-hour forecasting with a total sky imager at the UC San Diego solar energy testbed, Solar Energy, doi:10.1016/j.solener.2011.08.025, 85(11), 2881-2893,2011.

Coimbra, C., Kleissl, J., and Marquez, R.: Overview of solar forecasting methods and a metric for accuracy evaluation, in: Solar Resource Assessment and Forecasting, edited by: Kleissl, J., Elsevier, Waltham, Massachusetts, 2013.

Hammer, A., Heinemann, D., Lorenz, E., and Lückehe, B.: Short-term forecasting of solar radiation: a statistical approach using satellite data, Solar Energy, 67, 139–150, 1999.

Hinkelman, L., George, R., Wilcox, S., and Sengupta, M.: Spatial and temporal variability of incoming solar irradiance at a measurement site in Hawaii, in: 91st American Meteorological Society Annual Meeting, 23–27 January 2011, Seattle, WA, United States, 2011.

Jiang, H., Xue, H., Teller, A., Feingold, G., and Levin, Z.: Aerosol effects on the lifetime of shallow cumulus, Geophys. Res. Lett., 33, L14806, doi:10.1029/2006GL026024, 2006.

Lave, M. and Kleissl, J.: Cloud speed impact on solar variability scaling – application to the wavelet variability model, Sol. Energy, 91, 11–21, doi:10.1016/j.solener.2013.01.023, 2013.

Lave, M., Kleissl, J., and Stein, J.: A Wavelet-based Variability Model (WVM) for solar PV powerplants, IEEE Transactions on Sustainable Energy, 99, doi:10.1109/TSTE.2012.2205716, 4(2), 501-509, 2012.

Lave, M., Stein, J., and Kleissl, J.: Quantifying and simulating solar power plant variability using irradiance data, in: Solar Resource Assessment and Forecasting, edited by: Kleissl, J., Elsevier, Waltham, Massachusetts, 2013.

Leese, J. A., Novak, C. S., and Clark, B. B.: An automated technique for obtaining cloud motion from geosynchronous satellite data using cross correlation, J. Appl. Meteorol., 10, 118–132, 1971.

Lorenz, E., Hammer, A., and Heinemann, D.: Short term forecasting of solar radiation based on satellite data, in: Proceedings of the ISES Europe Solar Congress EUROSUN2004, Freiburg, Germany, 20–24 June, 2004.

Perez, R., Kivalov, S., Schlemmer, J., Hemker Jr., K., Renné, D., and Hoff, T. E.: Validation of short and medium term operational solar radiation forecasts in the US, Solar Energy, 84, 2161–2172, 2010.

Urquhart, B., Ghonima, M., Nguyen, D., Kurtz, B., Chow, C. W., and Kleissl, J.: Sky imaging systems for short-term forecasting, in: Solar Forecasting and Resource Assessment, edited by: Kleissl, J., Elsevier, Waltham, Massachusetts, 2013.

Weigl, T., Nagl, L., Weizenbeck, J., Zehner, M., Augel, M., Öchsner, P., Giesler, B., Becker, G., Mayer, O., Betts, T., and Gottschalg, R.: Modelling and validation of spatial irradiance characteristics for localised irradiance fluctuations and enhancements, in: 27th European Photovoltaic Solar Energy Conference, 24–28 September, Frankfurt, Germany, 3801–3804, 2012.

Yang, H., Chow, C. W., Ghonima, M., Kurtz, B., Nguyen, D., Urquhart, B., and Kleissl, J.: Solar irradiance forecasting using a ground-based sky imager developed at UC San Diego, Solar Energy, 103: 502-524, 2014.